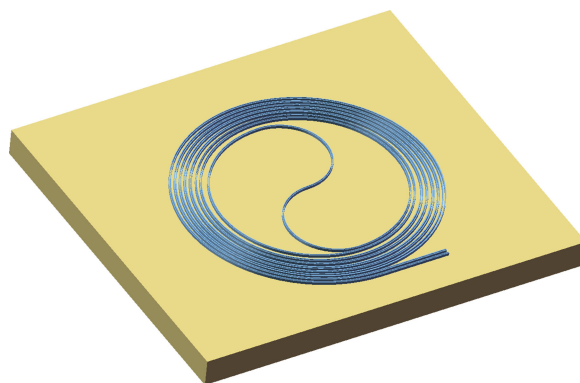


Integrated Optical Filter Using Spiral-Based Cascaded Mach–Zehnder Interferometers






Volume 11, Number 5, October 2019

Zhiqiang Ge
Chao Zeng
Yongkang Gong
Lingxuan Zhang
Guoxi Wang
Leiran Wang
Qibing Sun
Jinhai Si
Wei Zhao
Wenfu Zhang



DOI: 10.1109/JPHOT.2019.2940564

Integrated Optical Filter Using Spiral-Based Cascaded Mach–Zehnder Interferometers

Zhiqiang Ge ^{1,2,4}, Chao Zeng ¹, Yongkang Gong,³
Lingxuan Zhang ¹, Guoxi Wang,^{1,4} Leiran Wang ^{1,4}, Qibing Sun,¹
Jinhai Si ², Wei Zhao,^{1,4} and Wenfu Zhang ^{1,4}

¹State Key Laboratory of Transient Optics and Photonics, Xi'an Institute of Optics and Precision Mechanics, Chinese Academy of Sciences, Xi'an 710119, China

²Key Laboratory for Physical Electronics and Devices of the Ministry of Education and Shaanxi Key Lab of Information Photonic Technique, School of Electronic and Information Engineering, Xi'an Jiaotong University, Xi'an 710049, China

³School of Physics and Astronomy, Cardiff University, Cardiff CF24 3AA, U.K.

⁴University of Chinese Academy of Sciences, Beijing 100049, China

DOI:10.1109/JPHOT.2019.2940564

This work is licensed under a Creative Commons Attribution 4.0 License. For more information, see <https://creativecommons.org/licenses/by/4.0/>

Manuscript received August 25, 2019; accepted September 6, 2019. Date of publication September 10, 2019; date of current version October 1, 2019. This work was supported in part by National Natural Science Foundation of China (NSFC) under Grants 61675231, 61635013, 61705257, and 61805277; in part by the Strategic Priority Research Program of the Chinese Academy of Sciences under Grant XDB24030600; and in part by Youth Innovation Promotion Association of CAS under Grant 2016353. Corresponding author: Wenfu Zhang (e-mail: wfuzhang@opt.ac.cn).

Abstract: We have proposed a new compact integrated optical filter based on cascaded Mach-Zehnder interferometers (MZIs), and designed corresponding coupling structures without S-bend. The wavelength dependence and fabrication tolerance of coupling structures constructed in straight waveguides and bent waveguides were sufficiently analyzed by the finite-difference time-domain (FDTD) method. The results showed that the curved coupler possesses property of broadband with large fabrication tolerance. Specifically, for the presented 3 dB coupler incorporated with the asymmetric curved waveguides, the deviation of transmission remained below 2% at wavelength from 1.5 to 1.6 μm , which is greatly helpful to broadband spectral response of cascaded MZIs. By connecting curved couplers with spiral waveguides, a filter by means of two-stages cascaded MZIs was optimally demonstrated to realize a channel spacing of 10 nm. The spiral-based MZIs filter (SBMF) provides a new reference for MZIs filter limited by footprint and wavelength dependence.

Index Terms: Cascaded Mach-Zehnder interferometers, curved coupler, filter, spiral waveguide, wavelength-division demultiplexers, wavelength dependence.

1. Introduction

Wavelength-Division-Multiplexed (WDM) system [1] plays an important role in optical communications, and filter components are basic elements in WDM system, which select individual wavelength channels from signal stream [2]. Currently, researchers have paid attention to lots of approaches, such as arrayed-waveguide grating [3], grating-assisted coupling structures [4], [5], micro-ring resonators [6], and MZI or cascaded MZIs [7], [8]. One MZI is realized by connecting directional couplers (DCs) with an optical delay line. By employing a MZI or cascaded MZIs, some functional devices, such as the narrow-band interleavers [9], flat-top passband coarse wavelength-division multiplexer

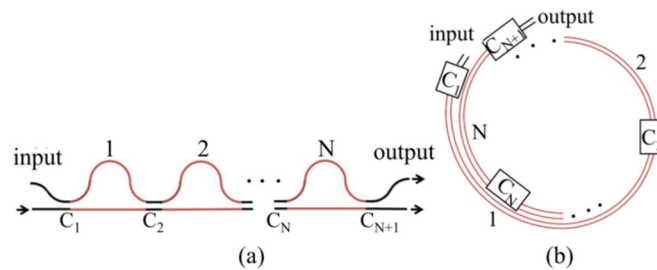


Fig. 1. Cascaded MZIs based on (a) directional form and (b) spiral waveguides.

(CWDM) [10], can be obtained optimally. While the MZIs circuits are popular for wavelength-selective operation with relatively weak sensitivity to fabrication errors, the sensitivity of DCs to fabrication errors and footprint of the cascaded circuit are in sore need of further reduction for compact integrated optical interconnects.

Generally, footprint of planar lightwave circuit (PLC) is mainly determined by two factors: bend radius and components complexity. Nevertheless, under the two factors unchanged, a superior layout alternative would be effective to meet requirements for footprint in terms of special occasions. For instance, an Archimedean spiral cavity to replace a racetrack resonator was implemented for an ultra-compact optical comb filter [11]. For cascaded MZIs, Fig. 1(a) shows the directional form of typical scheme. It is known that the amount of filter stages is related to filter finesse [7], and the cascaded MZIs filters with several stages are often used [12]. Hence, device length in the direction of light propagation is determined by the number of stages (commonly several millimeters) [13], especially for large numbers of stages or large phase delay, the length of conventional cascaded MZIs filter will increase rapidly with the increment of stages and phase delay [7].

In order to enlarge target applications of cascaded MZIs filter, and at least get rid of the limitation associated with device length in the direction of light propagation. We tended to ingeniously address phase delay by difference between inner radius and outer radius of parallel spiral waveguides. In this way, when the number of stages and phase delay augment, more circles can bring enough phase delay and allow many stages at a lower footprint cost, which is a relatively small addition on footprint compared with that in Fig. 1(a). Moreover, the inputs and outputs can easily be placed at the same side due to spiral waveguides, which caters for needs of packaging that it is often desired that both inputs and outputs are located at the same side. Typically aiming to the based-spiral device, we also uniquely proposed the curved coupler without S-bend to cooperate with spiral waveguides. Significantly, by sufficiently studying the wavelength dependence and fabrication tolerance of the arched coupler, as is expected that optical response has great insensitivities to wavelength and fabrication errors. Therefore in this paper, a new-type of cascaded MZIs filter based on spiral waveguides was proposed and investigated as depicted in Fig. 1(b). Despite of slight increase of footprint on width, it is notable that the cost has an exchange for considerable reduction of device length, and thus provides feasible solutions when device length is seriously limited. Specifically, a SBMF with two stages was carried out to adequately demonstrate the considerable potential for possible application on compact MZIs filter.

2. Design of a Unique Broadband Coupler Based on Curved Waveguide

Firstly as shown in Fig. 2, the coupling configuration based on DC was investigated to propose a unique curved coupler without S-bend, which is desired to properly match with spiral waveguides for a complete SBMF. Successively, the configuration was introduced into parallel curved waveguides with different bend radii, and characteristic of the asymmetric curved coupler, including wavelength dependence and fabrication tolerance, was analyzed. In analysis, considering the birefringence effect of guided modes in waveguides, the structures were designed for TE-polarization modes and studied for coupling, sensitivities to wavelength and fabrication errors. In Fig. 2, the waveguides

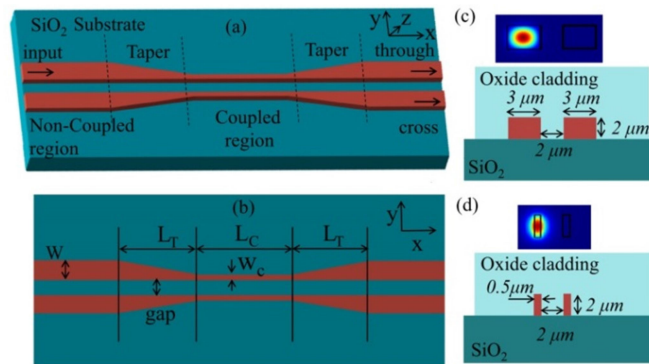


Fig. 2. Schematic of the proposed structure for (a) perspective view, (b) top view, (c) cross-section view of the non-coupled region, (d) cross-section view of the coupled region.

are on the SiO_2 substrate, and they are covered by an oxide cladding. The structure constructed in two parallel straight waveguides is divided into the non-coupled region and coupled region by the taper sections. For the non-coupled region, the core width of waveguide was uniquely designed to remain relatively a broad value. This is precisely to effectively ensure the guided mode confined tightly as shown in the inset of Fig. 2(c).

Furthermore, the more gap between waveguides is, the smaller overlap between guided modes invariably becomes. Thus, the large enough gap ($2 \mu\text{m}$) was properly chosen to prevent guided modes from being coupled. On the contrary, for the coupled region, while the gap between parallel waveguides keeps constant, by means of a taper section, mode profile can be moved laterally by adequately controlling the core width of waveguides, which tremendously improves the overlap between guided modes. Meanwhile, when the core width decreases, the local confinement of guided mode will be relaxed to enhance the coupling between waveguides in the coupled region. According to the fundamental principle, the presented structure in Fig. 2 can realize power splitting without a typical S-bend [14]. In this academic work, a 3D FDTD model was built and analyzed by the commercial software Photon Design [15] based on finite-difference time-domain (FDTD) method. The refractive indices of waveguide and suitable substrate/oxide cladding are 1.6 and $n_{\text{SiO}_2} = 1.45$ respectively. To properly obtain strong confinement for the guided modes (fundamental TE modes) in waveguides of the non-coupled region as Fig. 2(c), we carefully chose the core width of $3 \mu\text{m}$ to dramatically decrease field distribution outside the waveguides when the gap of $2 \mu\text{m}$ was set to implement extremely weak overlap of guided modes in the non-coupled region, whereas the core width of waveguide in the coupled region decreased to $0.5 \mu\text{m}$ to promote overlap of guided modes under the constant gap in the inset of Fig. 2(d). As is shown in the field distribution of Fig. 2(c) and Fig. 2(d) that the overlap of guided modes can be calculated as 1.487×10^{-6} for prevailing TE_0 mode in the non-coupled region, which is negligible compared with that (0.061) of TE_0 modes in the coupled region. Based on the symmetric coupling configuration, a 3 dB coupler was designed with the tapering length ($L_T = 86 \mu\text{m}$) and coupling length ($L_C = 24 \mu\text{m}$) respectively. At the wavelength of $1.55 \mu\text{m}$, the field distribution of $E_y(x, y)$ for fundamental TE mode was calculated in Fig. 3, which exhibits 3 dB power splitting.

Currently, the concerted efforts have been invested to enlarge bandwidth and fabrication tolerance by introducing the asymmetric structures. Some of them are referred to as the couplers between curved waveguides [16], [17], also some are referred to as the coupling amidst the tapered silicon-on-insulator (SOI) nanowire with little gap [18], [19], or coupling between silicon hybrid plasmonic waveguide and silicon waveguide [20], [21]. This reveals the possibility of implementing broadband and easy fabrication by altering typical symmetric structure. Thus promptly taking advantage of asymmetric curved waveguides, the curved coupler without S-bend was proposed within the above coupling mechanism in Fig. 4, and then the characteristics were investigated numerically. On one hand, compared with the symmetric structure in Fig. 2, it is the most key point that the

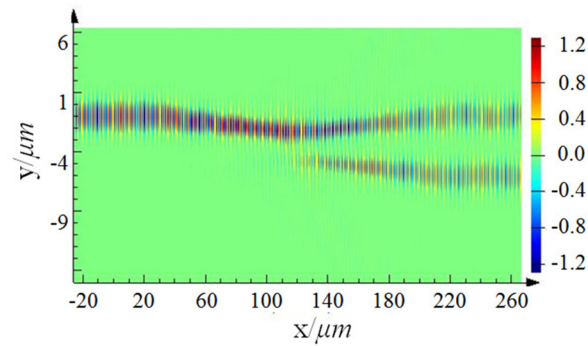


Fig. 3. Field distribution of 3 dB coupler based on the proposed structure without S-bend in Fig. 2.

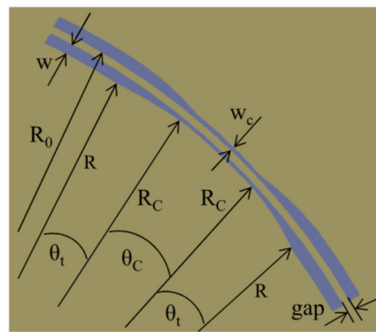


Fig. 4. Schematic of the proposed curved coupler with the invariant gap.

parallel curved waveguides provide the asymmetric characteristic, which results in an impressive performance of curved coupler in wavelength dependence and fabrication tolerance [17]. This is theoretically consistent with the conclusions of past studies. On the other hand, compared with the conventional DC with a S-bend, the proposed curved coupler without a typical S-bend could be perfectly embedded in the parallel spiral waveguides and makes the SBMF compact. In Fig. 4, the two waveguides are arranged parallel to each other in proximity of the gap, and bend by the radius of $R + w + \text{gap}/2$. With different radii ($R_1 = R + w/2$ and $R_2 = R_0 + w/2$), the two parallel waveguides taper from non-coupled region into coupled region, and the core width varies appreciably from w to w_c . Here, R_0 is defined as $R_0 = R + w + \text{gap}$. In the following discussions, some proper settings are required to reduce selected variables appropriately. To begin with, the core widths of waveguides in the non-coupled region and the gap keep the same as those of the above structure in Fig. 2 ($w = 3 \mu\text{m}$ and $\text{gap} = 2 \mu\text{m}$). Secondly, the core widths of two curved waveguides in the coupled region remain steadfastly and are succinctly described by the coupling width w_c . Thirdly, the two taper sections are on the symmetry of the coupled region. Moreover, both inner and outer taper sections possess the same angle θ_t . Finally, it is known that bend loss of curved waveguide depends on its radius seriously [22]. To ensure smaller bend loss, the bend radius is analyzed and chosen at least $\sim 300 \mu\text{m}$ for all curved waveguides.

It is noted that due to different bend radii in the two waveguides, the curved coupler can provide the differences of propagation constants of modes in spite of the same waveguide width. In the non-coupled region, effective refractive indices of guided modes are different to result in the phase mismatch. It promotes the non-coupling between the waveguides, and this is what we expect. For the coupled region, it can be found that the phase mismatch exerts direct influence on maximum coupling ratio, but this can be modified by optimizing the core width of waveguides to achieve phase match condition in the coupled region [23]. We have also discussed the effects of tapering

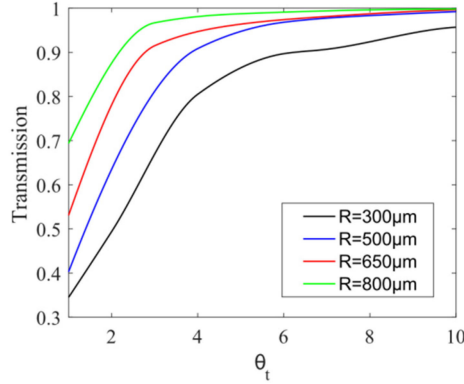


Fig. 5. Characteristic of taper section with tapering angle θ_t in Fig. 4. Relationship between the tapering angle θ_t and transmission with different radius R , while waveguide width w and coupling width w_c are chosen to be $3 \mu\text{m}$ and $0.5 \mu\text{m}$ respectively, at the wavelength of $1.55 \mu\text{m}$.

angle θ_t and bend radius R on maximum coupling ratio for the curved coupler. This indicates that the structural parameters can be designed to achieve desired splitting ratio. Therefore, in spite of the invariant gap, the curved coupler can be reasonably expected to perform the same operation as asymmetric coupler. Moreover, it can generate weak dependence of coupling characteristic on wavelength and fabrication errors due to the asymmetry.

According to the coupled-mode theory [24], the output power of DC is represented by

$$P_{\text{Through}} = P_{\text{in}} \left[1 - \left(\frac{k_c}{K} \right)^2 \sin^2(K \cdot L) \right]$$

$$P_{\text{Cross}} = P_{\text{in}} \left(\frac{k_c}{K} \right)^2 \sin^2(K \cdot L) \quad (1)$$

Here, P_{Through} and P_{Cross} are the output power of through port and cross port respectively, k_c is coupling coefficient, K is expressed by

$$K = \sqrt{\left(\frac{\beta_1 - \beta_2}{2} \right)^2 + k_c^2} \quad (2)$$

Here, β_1 and β_2 are the propagation constants of two guided modes in waveguides respectively. The proportional amplitude term of $(k_c/K)^2$ represents maximum coupling ratio between two waveguides. For symmetric coupling structure, the effective refractive indices of two guided modes are the same in the symmetric waveguides, which means $\beta_1 = \beta_2$. Thus the proportional amplitude term of $(k_c/K)^2$ can reach 100%. However, due to the periodical 100% power coupling between two waveguides, the conventional coupler (symmetric structure) is inherently highly sensitive to the wavelength. On the contrary, because of the asymmetric characteristic of the curved coupler, effective refractive indices in the two waveguides differ remarkably to properly lead the different propagation constants ($\beta_1 \neq \beta_2$). Thus, the maximum coupling ratio is hard to be 100%, which means that input power is not completely transferred to another specific output. The coupling ratio varies sinusoidally between 0 and maximum coupling ratio as the coupling length (θ_c) varies. For the proposed curved coupler, the maximum coupling ratio can be optimized from 0 to 1 by modifying bend radius R , tapering angle θ_t and coupling width w_c , which could be carefully designed for desired splitting power. This is to ensure that maximum coupling ratio $(k_c/K)^2$ is equal to (or slight above) desired splitting power while coupling length (θ_c) is chosen correctly at (or slightly more than) the peak of the sinusoid. As a fundamental link between the coupled region and non-coupled region, the taper section of curved coupler was firstly explored. As shown in Fig. 5, transmission monotonically

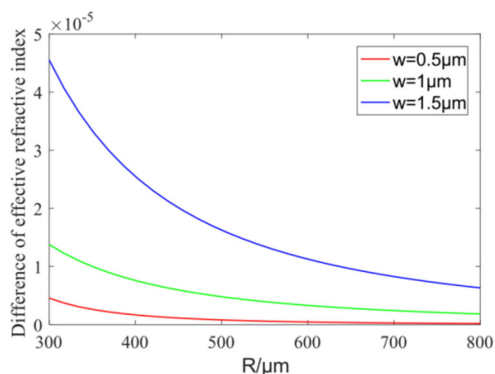


Fig. 6. Phase match of modes between two parallel curved waveguides in Fig. 4. At the wavelength of $1.55 \mu\text{m}$, differences of effective refractive indices of TE fundamental modes between two parallel curved waveguides while inner waveguide radius is $R + w/2$ and outer waveguide radius is $R + w + \text{gap} + w/2$ under $\text{gap} = 2 \mu\text{m}$.

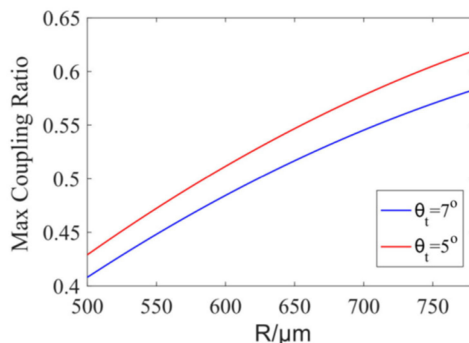


Fig. 7. Max coupling ratio with respect to bend radius R respectively at $\theta_t = 7^\circ$ and $\theta_t = 5^\circ$ for the wavelength of $1.55 \mu\text{m}$ when waveguide width w and coupling width w_c are $3 \mu\text{m}$ and $0.5 \mu\text{m}$, and gap is $2 \mu\text{m}$ for the proposed curved coupler in Fig. 4.

increases as θ_t varies from 2° to 10° , which accords with that of straight tapering structures. This is invariably because of the more suitable match of modes between cross sections in the direction of optical propagation when tapering length gets longer. For curved waveguide, bend radius has a considerable influence on transmission of taper section. When optical mode propagates along bent waveguide, guided mode will move laterally. The smaller the bend radius is, the stronger the effect is. If more portion of electric field is adequately maintained in the waveguide, the bend loss would decrease substantially [25]. Hence, a big radius is helpful to reduce loss. For this design, when R is above $500 \mu\text{m}$ and θ_t is larger than 8° , the transmission relatively approaches to 100%. In Fig. 6, differences of effective refractive indices for TE₀ modes in the two waveguides have been reasonably calculated to sufficiently demonstrate potential effect of R and w on phase match when inner waveguide radius is $R + w/2$ and outer waveguide radius is $R + w + \text{gap} + w/2$ ($\text{gap} = 2 \mu\text{m}$). It can be observed that the curves drop gradually as the bend radius increases, and slope gets smaller and smaller. Moreover, when waveguide width w decreases, the difference typically reduces, which means that β_1 is closer to β_2 . The better phase match can distinctly promote maximum coupling ratio between two curved waveguides. Therefore, we can positively enhance maximum coupling ratio of the curved coupler by adopting smaller w_c or bigger R . It is demonstrated in Fig. 7 that increasing radius R can enable high maximum coupling ratio because of reduction of difference of effective indices between two waveguides with the same width. In addition, we have found the effect of θ_t on maximum coupling ratio. Taking $\theta_t = 5^\circ$ and 7° as examples respectively, we can see that

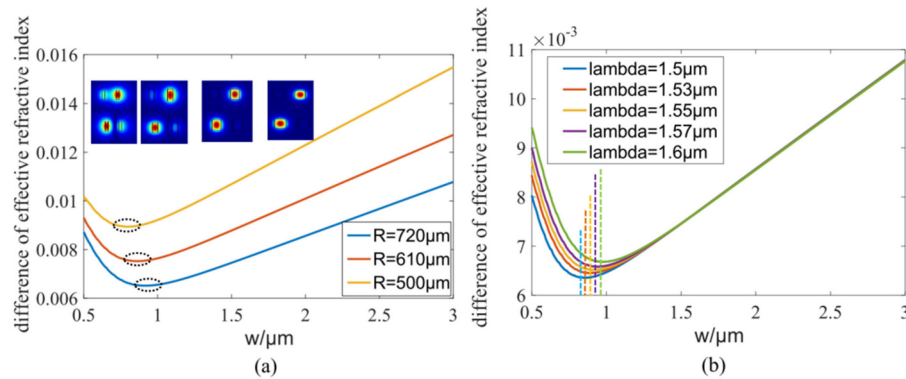


Fig. 8. Differences of effective refractive indices of two supermodes in the taper sections with respect to waveguide width ranging from 0.5 to 3 μm for (a) $R = 500, 610, 720 \mu\text{m}$ respectively as shown in Fig. 4 and (b) different input wavelengths under $R = 720 \mu\text{m}$.

the maximum coupling ratio of $\theta_t = 5^\circ$ is more (2% \sim 5%) than that of $\theta_t = 7^\circ$. In other words, minor tapering length can help improve the maximum coupling ratio. For taper sections, the difference of effective indices will be gradually augmented as the waveguide width ranges from w_c to w . When the length of tapering region within the weak match is shortened, there will be no sufficient length for optical interacting with each other under weak match. Extremely, if disregarding violent losses of taper sections to appreciably reduce the angle θ_t to remain a very small value, optical coupling is negligible in the taper sections, which is similar to function of S-bend design in conventional DCs. At this time, the significant coupling behavior primarily happens in the coupled region, in which the smallest width w_c brings the best phase match. Importantly, with increasing of waveguide width in the tapers, the mode field overlap will rapidly become weak according to the couple-mode theory. Thus we can obtain maximum coupling ratio as higher as possible. This is why smaller θ_t can result in higher maximum coupling ratio for the curved coupler. Meanwhile, considering the effect of the tapering length on transmission and maximum coupling ratio as shown in Fig. 5 and Fig. 7, there exists a trade-off between them when designing the angle θ_t . According to the desired coupling ratio and average loss, we can carefully choose appropriate R and θ_t to realize a curved coupler.

Apart from effect of phase mismatch on the coupling characteristic, we should also note that because overlap of guided modes between the two bent waveguides becomes small as the widths of waveguides vary from w_c to w , the coupling coefficient between the two waveguides decreases gradually. Hence, considering that both modes overlap and phase mismatch are related with waveguide width, supermodes in the taper sections were calculated to unveil coupling mechanism in Fig. 8 when the width varies from $w_c = 0.5 \mu\text{m}$ to $w = 3 \mu\text{m}$ under $gap = 2 \mu\text{m}$. Firstly, crucial influence of bend radius R on coupling coefficient was studied in Fig. 8(a). It can be seen that larger R corresponds to smaller difference of effective refractive indices of supermodes, which means weak coupling between the two waveguides. Moreover, it was also found that there exists a minimum point for each curve, which is marked by a black circle in Fig. 8(a). The waveguide width, corresponding to one black circle, is defined as w_m . When waveguide width increases from 0.5 μm to w_m , the gradual decline of curve indicates decreasing of coupling coefficient. However, when waveguide width is larger than w_m , the curve goes up with increasing of waveguide width, and the two lowest order modes tend to propagate independently as shown in the insets of Fig. 8(a). For $R = 720 \mu\text{m}$, the field distributions of the two modes respectively at $w = 0.5 \mu\text{m}$, 0.8 μm , 1.5 μm , and 2 μm , were calculated and exhibited from left to right in Fig. 8(a). It can be seen that the coupling becomes weak as the waveguide width increases. Especially for width approaching to 3 μm , the main fields of two modes are respectively confined in the two different waveguides and the coupling gets so weak as to be negligible, which successfully achieves power splitting under invariant gap. We defined w_m as coupling cut-off point. One can see that the point moves left slightly

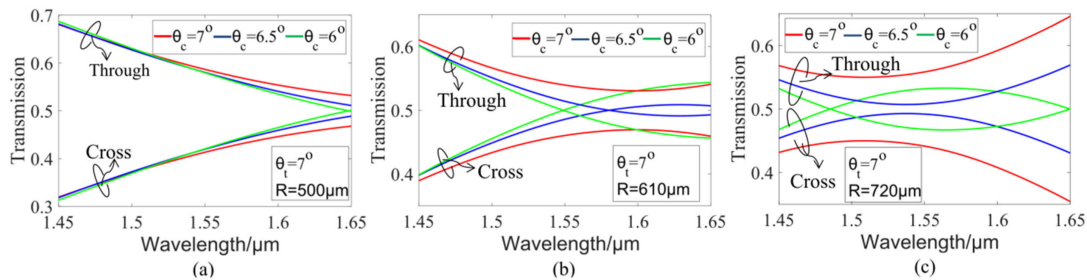


Fig. 9. Effect of the coupling angle θ_c on spectral response under $w = 3 \mu\text{m}$, $w_c = 0.5 \mu\text{m}$, $\theta_t = 7^\circ$, $\text{gap} = 2 \mu\text{m}$ when (a) $R = 500 \mu\text{m}$, (b) $610 \mu\text{m}$, (c) $720 \mu\text{m}$.

when the radius R reduces, which implies that the coupling behavior in the taper sections stops at smaller waveguide width. Meanwhile, the effect of input wavelength on coupling coefficient was also analyzed carefully. Under $R = 720 \mu\text{m}$, differences of effective refractive indices were calculated for different wavelengths. It is shown in Fig. 8(b) that the longer the input wavelength, the bigger difference of effective refractive indices, which results in smaller coupling length. In addition, as is displayed by the positions marked in the dashed lines, coupling cut-off point also moves right slightly when input wavelength increases from 1.5 to 1.6 μm . Nevertheless, all of them are situated in the width of $\sim 1 \mu\text{m}$.

For the curved coupler, the spectral responses, including the peaks of transmission and the wavelengths at the peaks, are significantly influenced by the coupling angle θ_c and R . The dependence of transmission on θ_c has been calculated in Fig. 9. These results were obtained by changing θ_c under $\theta_t = 7^\circ$ and $R = 500, 610, 720 \mu\text{m}$ respectively. The coupling angle increases from $\theta_c = 6^\circ$ to $\theta_c = 7^\circ$ by increments of 0.5° . It is easy to note that when improving θ_c , the peak of transmission in cross port reduces and the area of the intersection between the two curves for through port/cross port shrinks. The Figs. 9(b) and 9(c) exhibit that there is no intersection between two curves for $\theta_c = 7^\circ$. Importantly, the wavelength at peak providing wavelength insensitive operation is also shifted. We can see slight blue shift of spectral peak position with increase of θ_c . Meanwhile, the R can also shift the wavelength of peak to acquire broadband operation in the desired wavelength region. The phenomenon can be caused by the two factors. Those are the effects of bend radius and wavelength on difference of effective indices between two supermodes as shown in Fig. 8. Coupling length will increase as R becomes large. However, the increment of coupling length is less than that of length of coupled region. Additionally, enhancing wavelength can enlarge difference of effective indices, which means that longer wavelength can shorten coupling length. Consequently, enhancing bend radius can boost blue shift of spectral peak position as depicted in Fig. 9(a)–(c). Obviously, by optimizing appropriate θ_c and R to put working wavelength at the position of spectral peak, the wavelength dependence of transmission response can be suppressed effectively in the curved coupler.

Successively, the broadband 3 dB curved coupler was proposed and the numerical investigation of wavelength dependence was completed as shown in Fig. 10(a). Considering the effects of θ_t/θ_c on maximum coupling ratio/spectral peak as shown in Figs. 7/9, we finally obtained the proper parameters by parameter sweep and optimization. The θ_t and θ_c were designed to be 7° and 6.41° when the R was chosen to be $720 \mu\text{m}$. It can be seen that in the wavelength range from 1.5 to 1.6 μm , the standard deviation of transmission is less than 2% compared with that at the center of 1.55 μm . Especially from 1.54 to 1.56 μm , wavelength dependence is strongly restrained to keep 3 dB power splitting. Compared with coupling characteristic of symmetric DCs, the broadband is easy to be obtained for the curved coupler. To prove it, the 3 dB coupler at 1.55 μm was designed based on the symmetric structure in Fig. 2 and spectral response of the 3 dB coupler was calculated in Fig. 10(b). The result shows that from the wavelength of 1.5 to 1.6 μm , the deviation of transmission maintains approximately $\pm 10\%$. Therefore, the considerable enhancement on operational bandwidth can be realized by employing the curved coupler.

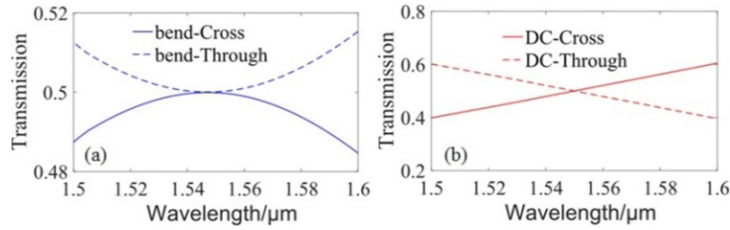


Fig. 10. Wavelength dependence of (a) the 3 dB curved coupler under $R = 720 \mu\text{m}$, $w = 3 \mu\text{m}$, $\theta_t = 7^\circ$, $w_c = 0.5 \mu\text{m}$, $\theta_c = 6.41^\circ$, $\text{gap} = 2 \mu\text{m}$, and (b) the 3 dB coupler based on the symmetric structure in Fig. 2 at $L_T = 86 \mu\text{m}$, $L_C = 24 \mu\text{m}$.

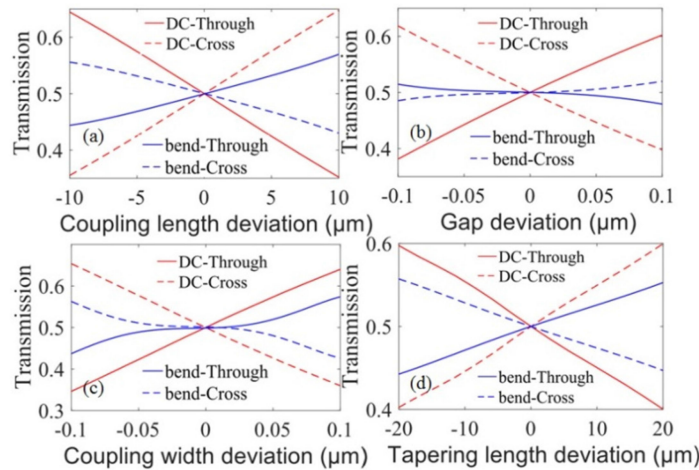


Fig. 11. Fabrication tolerance of the 3 dB curved coupler with $R = 720 \mu\text{m}$, $w = 3 \mu\text{m}$, $\theta_t = 7^\circ$, $w_c = 0.5 \mu\text{m}$, $\theta_c = 6.41^\circ$, $\text{gap} = 2 \mu\text{m}$ and the 3 dB symmetric coupler of Fig. 2 with $L_T = 86 \mu\text{m}$, $L_C = 24 \mu\text{m}$ for (a) coupling length, (b) gap, (c) coupling width, (d) tapering length.

Additionally, the fabrication tolerances of the 3 dB curved coupler and the 3 dB symmetric coupler were precisely calculated and carefully analyzed in Fig. 11. For curved coupler, the coupling angle deviation is depicted by $\Delta\theta$ and coupling length deviation ΔL is approximately expressed by $\Delta L = \Delta\theta \cdot R$ in Fig. 11(a). Here, the R is $720 \mu\text{m}$. The tapering length deviation was also calculated by using this method. One can observe that splitting ratio of the 3 dB curved coupler is clearly insensitive to fabrication error. Especially for the gap deviation and the coupling width deviation of $\pm 50 \text{ nm}$, the transmission deviation keeps at $\sim \pm 1\%$. It should be mentioned that under the θ_t of 7° , the maximum coupling ratio of $\sim 56\%$ is determined when the R is $720 \mu\text{m}$ according to Fig. 7. The desired 3 dB splitting ratio is less than the maximum coupling ratio, so the designed θ_c is larger than that corresponding to the maximum coupling ratio as depicted in Fig. 11(a). If the fabrication tolerance of coupling length is expected to have a better performance, an effective way is by increasing θ_t or reducing R to decrease maximum coupling ratio to 50%. Hence, in addition to weak wavelength dependence of coupling characteristic, the curved coupler has significant potential in large fabrication tolerance.

3. Design of Spiral-Based MZIs Filter(SBMF)

In order to realize the SBMF, we have proposed the corresponding curved coupler with broadband and large fabrication tolerance, and analyzed effect of the structural parameters on the characteristic of transmission in the aforementioned contents. Therefore in this section, by connecting curved

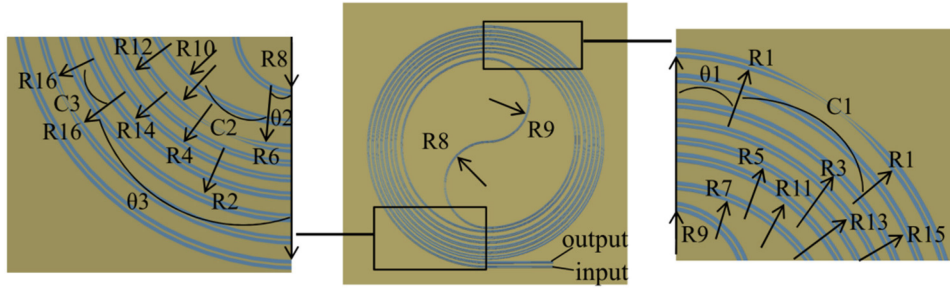


Fig. 12. Schematic of optimized SBMF with three curved couplers named C1, C2 and C3.

couplers with spiral waveguides, a complete circuit was correctly designed and carefully optimized to realize desired spectral response, and advantages on footprint of SBMF were precisely analyzed in contrast to conventional cascaded MZIs filter.

The cascaded MZIs operation can be described by using transmission matrices for the Mach-Zehnder and coupler sections. The transmission matrix of N -stages filter can be expressed as:

$$S = T_{N+1}(\lambda) \cdots T_{MZ} T_2(\lambda) T_{MZ} T_1(\lambda) \quad (3)$$

Where $T_N(\lambda)$ is the transmission matrix of the N th coupler [26]. Obviously, it is the function related with wavelength because the propagation constant varies with the wavelength [10]. Here, the weak wavelength dependence of coupler is desired to realize a better spectral response for wavelength-selective devices based on cascaded MZIs. The transmission matrix for the Mach-Zehnder two arm sections is expressed as:

$$T_{MZ} = \begin{bmatrix} \exp(j\Delta\phi/2) & 0 \\ 0 & \exp(-j\Delta\phi/2) \end{bmatrix} \quad (4)$$

Where $\Delta\phi$ is optical path length difference between two branches (the inner waveguide and the outer waveguide in the scheme) [7]. For phase delay section of the proposed filter, the optical delay line δL , defined as length difference between two branches, could be naturally obtained due to difference between bend radii of inner waveguide and outer waveguide. Fig. 12 gives the schematic of SBMF with two stages. It is displayed that the R of waveguide gradually changes every 180 degree, and the R changes in the order of $R1$ to $R16$ as the light propagates. For every radius with 180 degree, the δL is calculated as $\pi(w + gap)$. Further, when the two parallel curved waveguides circle for N times, the δL is calculated as $2N\pi(w + gap)$, which indicates that the delay line just relies on waveguide width w and gap , and is not related with R . On the contrary, R is a key parameter for splitting ratio in Fig. 7. Thus we can choose the bend radius completely according to desired ratio and disregard the effect on delay line. This avoids some conflicts when choosing the proper R . It also should be noted that the additional N circles would increase the size of filter, but the footprint is improved in scale of N -times waveguide widths. This is the reason why for many stages, the SBMF can possess more compact footprint than that of conventional MZIs filter. In Fig. 12, the three curved couplers, named C1 (coupler1), C2 (coupler2) and C3 (coupler3), were respectively inserted into the SBMF. Their positions were described by $\theta1$ (5°), $\theta2$ (5°), $\theta3$ (44.5°), and the optimal results were exhibited in Fig. 13.

By utilizing the FDTD method, the spectral response of proposed SBMF was obtained as shown in Fig. 14. With the channel spacing of about 10 nm, the design has a good spectral performance in the wavelength range from 1.5 to 1.6 μm . Therefore, this demonstrated that it is feasible to realize compact MZIs filter working in a broadband wavelength range by the presented solution. The losses shown in Fig. 14 mainly come down to the following two points. Those are the losses introduced by tapers and overlap mismatch losses of two modes in interface between two spiral waveguides. Nevertheless, if needed, the losses can be drastically reduced by properly optimizing designs.

<i>symbol</i>	<i>Value/μm</i>	<i>symbol</i>	<i>Value/μm</i>	<i>symbol</i>	<i>Value/μm</i>
<i>R1</i>	780	<i>R8</i>	295	<i>R15</i>	745
<i>R2</i>	750	<i>R9</i>	290	<i>R16</i>	775
<i>R3</i>	720	<i>R10</i>	600	<i>w</i>	3
<i>R4</i>	690	<i>R11</i>	625	<i>w_c</i>	0.5
<i>R5</i>	660	<i>R12</i>	655	<i>gap</i>	2
<i>R6</i>	630	<i>R13</i>	685		
<i>R7</i>	605	<i>R14</i>	715		
		θ_t	θ_c	$R_c/\mu\text{m}$	
<i>Coupler1</i>		11°	4°	782.5	
<i>Coupler2</i>		8°	5°	632.5	
<i>Coupler3</i>		6.5°	0°	777.5	

Fig. 13. Table for structural parameters of the optimized SBMF in Fig. 12.

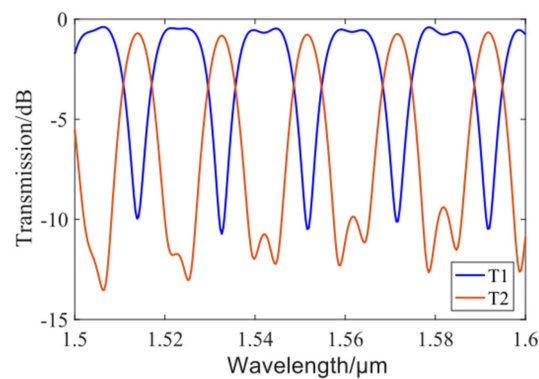


Fig. 14. Spectral response of the optimized SBMF in Fig. 12.

Finally, in order to prove advantage of SBMF on footprint, the conventional design based on cascaded MZIs was estimated and compared with the new scheme. Fig. 15 gives the schematic of delay section for conventional design, and the length of delay section is defined as L , which mainly determines length of the whole MZIs circuit. Hence, we just analyzed the effect of L on footprint, and ignored lengths of DC and S-bend design. But actually a lot of S-bend designs can also bring a relative large size for a N -stages filter. In Fig. 15(a), the up branch (green curve) simply comprises four same arcs with the radius R , and the delay line δL is represented by difference between the up branch (green curve) and the down branch (red curve). The relationship between the δL and length L in delay section has been calculated in Fig. 15(b). One can see that by increment of the δL , length L of the delay section gradually improves, and when the radius R grows, the delay section becomes long. To ensure a low bend loss, the minimum radius R_{min} was designed to be $\sim 300 \mu\text{m}$ in the SBMF of Fig. 12. When it is fair considered that bend radii of the arcs (green curve) are also chosen as $300 \mu\text{m}$, the length L of single delay section will range from 550 to $850 \mu\text{m}$ with respect to the δL from 20 to $100 \mu\text{m}$. For a N -stages filter, the length of conventional design will be estimated to be N -times length L at least when lengths of DCs and S-bend designs are disregarded. This means that the size of conventional design is seriously dependent on the amount N of cascaded stages so that large numbers of stages will make the device relatively long. On the contrary, the footprint of new scheme with N stages does not strongly depend on the amount N of stages, but the minimum bend radius R_{min} of waveguide situated in the center of circuit. With the increment of stages, the two parallel curved waveguides just need circular movement for a few more times. As a result, a

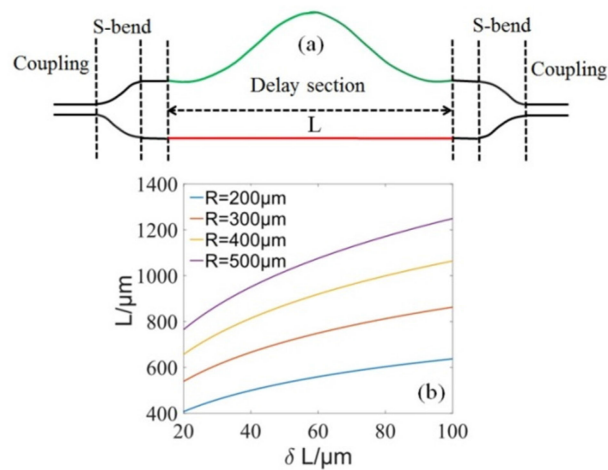


Fig. 15. (a) Schematic of delay section for conventional design and (b) effect of optical delay line δL on length L of delay section under different radii.

relatively small addition in the scale of dozens of waveguide widths is introduced into the footprint of the device with fundamental radius of $\sim 2R_{min}$. Although the fundamental radius makes the footprint of proposed SBMF on width slightly larger than that of conventional scheme, both length and width of the new scheme slowly grow with number of stages N . When beyond some stages N , the length of conventional scheme will greatly exceed that of new scheme due to the terrible growing, which reveals an improper application of conventional design on the layout limited on length. Therefore it is valuable that a slight addition of footprint on width has an exchange for considerable reduction of device length. However, it should be noted that this does not mean that length cost is transferred to width cost. Our work can dramatically reduce length under slow growing of width, and thus the advantage on footprint of SBMF gets remarkable when the amount of stages grows in a MZIs filter. Moreover, when also considering the minimum lossless radius, some other approaches, such as using spiral waveguide between MZIs as delay or rectangular-shape spiral devices, could not make it more compact.

4. Conclusion

In this paper, the SBMF with the potential of compact structure was proposed and investigated as the first of its kind to the best our knowledge. By employing the parallel curved waveguides, the corresponding curved coupler without S-bend was presented and analyzed to carry out the interesting project. Successively, connecting the curved couplers with spiral waveguides, a SBMF with two stages was achieved and optimized, and the spectral response was obtained. The proposed method can greatly decrease footprint (at least on device length especially for many stages) of MZIs filter. Meanwhile, the curved coupler has many structural parameters to be designed flexibly according to requirements while the response is insensitive to wavelength and fabrication errors. Therefore, the scheme provides a significant guidance for compact MZIs filter with many stages in optical communication.

References

- [1] I. P. Kaminow, "FSK with direct detection in optical multiple-access FDM networks," *IEEE J. Sel. Areas Commun.*, vol. 8, no. 6, pp. 1005–1014, Aug. 1990.
- [2] J. Stone and L. W. Stulz, "Pigtailed high-finesse tunable fiber Fabry–Perot interferometers with large, medium and small free spectral ranges," *Electron. Lett.*, vol. 23, no. 15, pp. 781–783, 1987.

- [3] H. Takahashi, S. Suzuki, K. Kato, and I. Nishi, "Arrayed-waveguide grating for wavelength division multi/demultiplexer with nanometre resolution," *Electron. Lett.*, vol. 26, no. 2, pp. 87–88, 1990.
- [4] Z. Ge *et al.*, "Low-threshold optical bistability in field-enhanced nonlinear guided-mode resonance grating nanostructure," *Opt. Lett.*, vol. 43, no. 17, pp. 4156–4159, 2018.
- [5] H. Sakata, "Sidelobe suppression in grating-assisted wavelength-selective couplers," *Opt. Lett.*, vol. 17, no. 7, pp. 463–465, 1992.
- [6] O. Tsilipakos, E. E. Kriezis, and S. I. Bozhevolnyi, "Thermo-optic microring resonator switching elements made of dielectric-loaded plasmonic waveguides," *J. Appl. Phys.*, vol. 109, no. 7, 2011, Art. no. 073111.
- [7] M. Kuznetsov, "Cascaded coupler Mach–Zehnder channel dropping filters for wavelength-division-multiplexed optical systems," *J. Lightw. Technol.*, vol. 12, no. 2, pp. 226–230, Feb. 1994.
- [8] H. H. Yaffe, C. H. Henry, M. R. Serbin, and L. G. Cohen, "Resonant couplers acting as add-drop filters made with silica-on-silicon waveguide technology," *J. Lightw. Technol.*, vol. 12, no. 6, pp. 1010–1014, Jun. 1994.
- [9] M. Oguma, K. Jinguiji, T. Kitoh, T. Shibata, and A. Himeno, "Flat-pass-band interleave filter with 200 GHz channel spacing based on planar lightwave circuit-type lattice structure," *Electron. Lett.*, vol. 36, no. 15, pp. 1299–1300, 2000.
- [10] Q. Wang and S. He, "Optimal design of planar wavelength circuits based on Mach–Zehnder interferometers and their cascaded forms," *J. Lightw. Technol.*, vol. 23, no. 3, pp. 1284–1290, Mar. 2005.
- [11] D.-X. Xu *et al.*, "Archimedean spiral cavity ring resonators in silicon as ultra-compact optical comb filters," *Opt. Exp.*, vol. 18, no. 3, pp. 1937–1945, 2010.
- [12] K. Jinguiji, N. Takato, Y. Hida, T. Kitoh, and M. Kawachi, "Two-port optical wavelength circuits composed of cascaded Mach–Zehnder interferometers with point-symmetrical configurations," *J. Lightw. Technol.*, vol. 14, no. 10, pp. 2301–2310, Oct. 1996.
- [13] D. W. Kim, A. Barkai, R. Jones, N. Elek, H. Nguyen, and A. Liu, "Silicon-on-insulator eight-channel optical multiplexer based on a cascade of asymmetric Mach–Zehnder interferometers," *Opt. Lett.*, vol. 33, no. 5, pp. 530–532, 2008.
- [14] J. Xing, Z. Li, X. Xiao, J. Yu, and Y. Yu, "Two-mode multiplexer and demultiplexer based on adiabatic couplers," *Opt. Lett.*, vol. 38, no. 17, pp. 3468–3470, 2013.
- [15] Photon Design. [Online]. Available: <http://www.photond.com/>. Accessed on: 2016.
- [16] D. Dai and J. E. Bowers, "Novel ultra-short and ultra-broadband polarization beam splitter based on a bent directional coupler," *Opt. Exp.*, vol. 19, no. 19, pp. 18614–18620, 2011.
- [17] H. Morino, T. Maruyama, and K. Iiyama, "Reduction of wavelength dependence of coupling characteristics using Si optical waveguide curved directional coupler," *J. Lightw. Technol.*, vol. 32, no. 12, pp. 2188–2192, Jun. 2014.
- [18] Z. Zhang, X. Hu, and J. Wang, "On-chip optical mode exchange using tapered directional coupler," *Sci. Rep.*, vol. 5, 2015, Art. no. 16072.
- [19] Y. Luo, Y. Yu, M. Ye, C. Sun, and X. Zhang, "Integrated dual-mode 3 dB power coupler based on tapered directional coupler," *Sci. Rep.*, vol. 6, 2016, Art. no. 23516.
- [20] F. Lou, D. Dai, and L. Wosinski, "Ultracompact polarization beam splitter based on a dielectric–hybrid plasmonic–dielectric coupler," *Opt. Lett.*, vol. 37, no. 16, pp. 3372–3374, 2012.
- [21] Y.-J. Chang and W.-L. Li, "Directional-coupler-based polarization splitting in asymmetric metal/multi-insulator configuration for optical nanocircuitry," *IEEE Photon. Technol. Lett.*, vol. 24, no. 5, pp. 458–460, Mar. 2012.
- [22] Z. Ge *et al.*, "On-chip router elements based on silicon hybrid plasmonic waveguide," *IEEE Photon. Technol. Lett.*, vol. 29, no. 12, pp. 952–955, Jun. 2017.
- [23] J. Liao *et al.*, "Mode splitter without changing the mode order in SOI waveguide," *IEEE Photon. Technol. Lett.*, vol. 28, no. 22, pp. 2597–2600, Nov. 2016.
- [24] H. Haus and W. Huang, "Coupled-mode theory," *Proc. IEEE*, vol. 79, no. 10, pp. 1505–1518, Oct. 1991.
- [25] D. Dai, Y. Shi, S. He, L. Wosinski, and L. Thylen, "Silicon hybrid plasmonic submicron-donut resonator with pure dielectric access waveguides," *Opt. Exp.*, vol. 19, no. 24, pp. 23671–23682, 2011.
- [26] H. Haus, *Waves and Fields in Optoelectronics*. Englewood Cliffs, NJ, USA: Prentice-Hall, 1984.